Design Methodology Using Magnetic Equivalent Circuit for an Integrated Magnetics Structure

Neha Rajput
Dept. of Electrical Engineering
Indian Institute of Science
Bengaluru, India
neharajput@iisc.ac.in

Vishnu Mahadeva Iyer
Dept. of Electrical Engineering
Indian Institute of Science
Bengaluru, India
vishnumi@iisc.ac.in

Gautham Ram Chandra Mouli
Faculty of EEMCS
Delft University of Technology
Delft, Netherlands
G.R.ChandraMouli@tudelft.nl

2025 IEEE Energy Conversion Congress & Exposition Asia (ECCE-Asia) | 979-8-3315-1886-8/25/$31.00 ©2025 IEEE | DOI: 10.1109/ECCE-Asia63110.2025.11112218

***Abstract*—The growing demand for compact, reliable, and high-efficiency power conversion systems has spurred the need for the development of power-dense magnetic solutions. This paper introduces a design algorithm utilizing an improved magnetic equivalent circuit (MEC) model for an integrated magnetic structure, which provides a more accurate and computationally efficient approach to capturing complex magnetic interactions. The proposed MEC-based design algorithm shows promising results in predicting the different reluctances, resulting in optimal magnetic design parameters. The effectiveness of the methodology is demonstrated through the design of an integrated structure for a 12.5 kW, 50 kHz dual-active bridge converter, wherein the energy-transfer series inductor and high-frequency transformer are seamlessly integrated into a single magnetic structure - hereafter referred to as the Integrated Magnetic Transformer (IMTx).**

***Index Terms*—Dual active bridge converter, Integrated magnetics structure, Magnetic equivalent circuit, Soft-ferrites.**

I. Introduction

The optimal design of magnetic components in a power electronics converter can be challenging but necessary, as they are responsible for approximately 40–50% of the converter weight and volume. Many power electronics converters rely on multiple magnetic components to function. Examples include dual-active bridge (DAB) converters [1] and LLC resonant converters [2] which typically comprise a series inductor and a high-frequency transformer. DC-DC converters that employ multiple inductors such as Cuk [3], SEPIC [4], or interleaved buck/boost topologies are also popular. In applications where space and volume are critical, integrated magnetics design concepts offer an alternative approach for converters with multiple magnetic components. While the concept of integrated magnetics is well-established [3], its applications are diverse and widespread. The well-established integration techniques involve the sharing of core or windings. In the former, multiple magnetic components share the same core while maintaining separate windings, reducing the core material usage and improving the power density requirements [5]. In contrast, in the latter, a single winding contributes to the magnetization of multiple magnetic components, reducing copper losses and improving efficiency [4].

Recent literature highlights several innovative integrated magnetic structures to enhance the performance of the DAB converter [6]–[10]. Integrating different magnetic components into a single core fosters improved efficiency and compactness and presents challenges, such as complicated and non-trivial design. Given that every power electronics converter has distinct operating waveforms and requirements, no integrated magnetic design can be considered universal. Reluctance modeling offers a rapid and direct approach to designing magnetic structures, but its complexity increases when dealing with integrated magnetic designs. To address this, accurately modeling the reluctance of air gaps, the window regions, and air reluctance inside and outside the core is crucial. This approach can enable the design of compact structures by developing a magnetic equivalent circuit (MEC). This paper presents a MEC-based design methodology for developing an integrated magnetic structure using ferrites for a 12.5 kW, 50 kHz dual-active bridge (DAB) converter. The integrated magnetic structure uses the transformer's leakage inductance as the energy transfer inductor, achieved through an external dedicated leakage path as shown in Fig. 1 [8], [11]. The paper discusses an improved MEC model and provides insights into the design of the integrated magnetic transformer (IMTx).

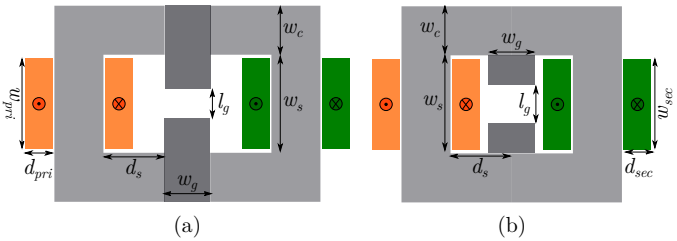

Fig. 1: Integrated designs of high-frequency transformer and energy-transfer series inductor of a dual-active bridge converter (a) IMTx 1 (b) IMTx 2. The IMTx 2 structure is a variation of the IMTx 1 architecture.

II. Steady-State Operation and Specifications of a Dual-Active Bridge Converter

This section briefly covers the steady-state operation of the DAB converter which will be utilized during the integrated magnetics design. The system specifications are 12.5 kW, 50 kHz, with input V_{in} and output V_o voltage levels of 750 V and 500 V, respectively. Analytically, the required leakage

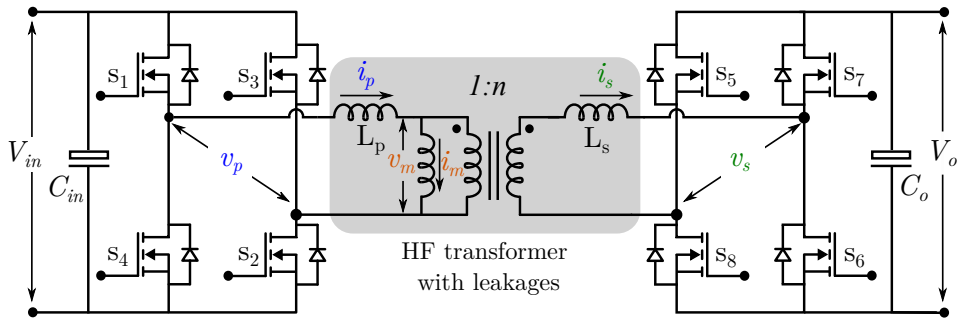

Fig. 2: Dual-active bridge converter with leakage inductances, L_p and L_s on both sides of the high-frequency (HF)transformer with finite magnetizing inductance L_m.

inductance L_{req} = 100 μH. The DAB converter consists of two H-bridges, each connected on either side of the transformer, and the leakage inductances L_p and L_s of the transformer realize the series inductance and act as the energy transfer component, as shown in Fig. 2. Each H-bridge's switching devices are driven such that they produce complementary square pulses. For RMS current minimization under single-phase shift modulation strategy [12], the expression for optimum equivalent duty $D(=\frac{2\beta}{\pi})$ is $1-\sqrt{1-\frac{4p_o}{m\pi}}$, where p_o is per-unit power transfer, m is the voltage conversion ratio and β is the phase shift between the ac voltages (v_p and v_s) across the bridge terminal of the two H-bridges. For $\beta=\frac{\pi}{2}$, the expression of maximum power transfer is given by

$$P_o = \frac{nV_{in}V_oT_sD(1-D)L_m}{2(n^2L_pL_m+L_sL_m+L_pL_s)} \tag{1}$$

in which n is the transformer turns ratio from secondary to primary side, V_{in} is the input voltage, V_o is the output voltage, T_s is the switching period, L_p and L_s are the leakage inductances on the primary and secondary sides of the high-frequency transformer, respectively, and L_m is the magnetizing inductance. The output current I_o can be regulated by controlling the phase shift β. The currents at the switching instants $t=t_1$ and $t=t_2$ can be derived and are given by and are indicated in Fig. 3

$$I_{p1} = \frac{V_{in}T_s((2D-1)(L_s+n^2L_m)+n^2ML_m)}{4(n^2L_pL_m+L_sL_m+L_pL_s)} \tag{2}$$

$$I_{p2} = \frac{V_{in}T_s(n^2(2D-1)(ML_m)+(L_s+n^2L_m))}{4(n^2L_pL_m+L_sL_m+L_pL_s)} \tag{3}$$

$$I_{s1} = \frac{nV_{in}T_s((2D-1)L_m+M(L_m+L_p)}{4(n^2L_pL_m+L_sL_m+L_pL_s)} \tag{4}$$

$$I_{s2} = \frac{nV_{in}T_s(M(2D-1)(L_m+L_p)+L_m)}{4(n^2L_pL_m+L_sL_m+L_pL_s)} \tag{5}$$

III. Integrated Magnetics Design Prototypes

A. Construction of Magnetic Equivalent Circuit (MEC)

The integrated design prototypes investigated in this work are depicted in Fig. 1. To increase the leakage inductance of a transformer, the primary and secondary windings, such as the side legs of the core, can be wound as far as possible.

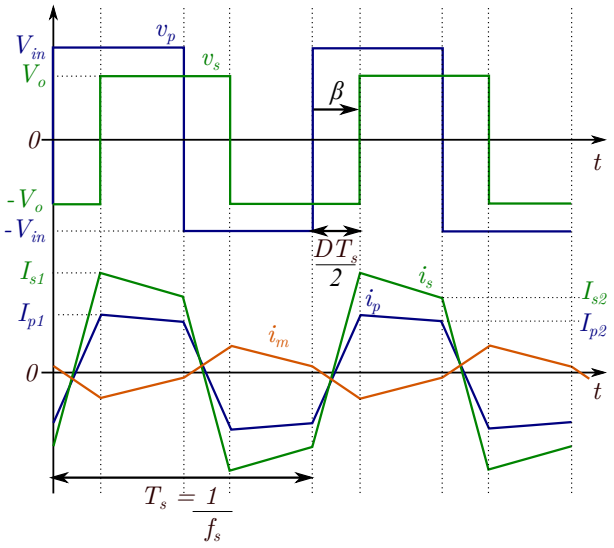

Fig. 3: Steady-state DAB converter waveforms under single-phase shift modulation strategy.

Another approach involves providing a leakage path at a suitable position; a regulated leakage inductance on either of the high-frequency transformer windings can be achieved [13]. Two possible strategies to incorporate the leakages are shown in Fig. 1. Both sides of the transformer will have equal leakage inductance due to the indicated leakage path's positioning. All the prototype designs are constructed using two U-cores and an I-core with d_c as the depth of the core. The *orange* equivalent foil conductor indicates the primary winding, and the secondary winding is indicated by the *green* conductor. Fig. 4 depicts the development of a magnetic equivalent circuit for designing prototype IMTx 1. The following steps are involved:

Case 1: $N_pI_p = N_sI_s$

First, the distribution of flux paths is considered under an equal MMF condition, wherein it is observed that the summation of $\phi_P^{'}$ and $\phi_S^{'}$ flux flows through the external leakage path; $\phi_l^{'} = \phi_P^{'} + \phi_S^{'}$ as indicated in Fig. 4(a).

Case 2: $N_pI_p > N_sI_s$ *or* $N_pI_p < N_sI_s$

Second, the distribution of flux paths is considered under unequal MMF conditions, wherein it is observed that a part

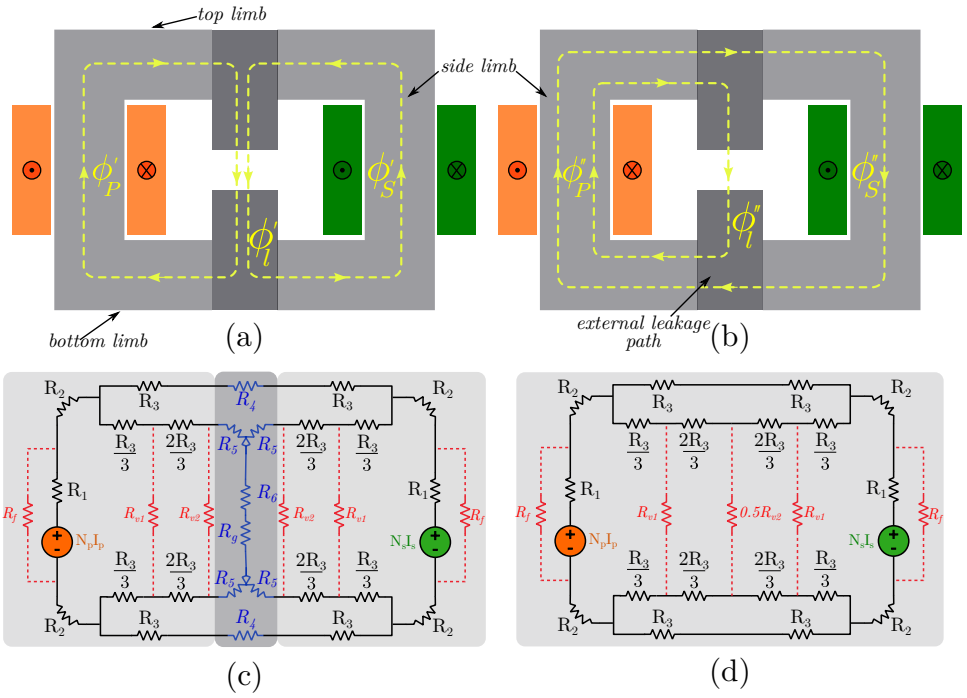

Fig. 4: Development of magnetic equivalent circuit (MEC) based on magnetizing flux paths (a) Equal MMFs $N_pI_p = N_sI_s$ (b) Unequal MMFs $N_pI_p > N_sI_s$ (c) MEC of IMTx 1 design incorporating the leakage (window, air-gap) reluctance paths as well (d) MEC of UU-core transformer without external leakage path.

of $\phi_P^{''}$ flows through the leakage path and the remaining flux through the other limb; $\phi_P^{''} = \phi_l^{''} + \phi_S^{''}$ for the example shown in Fig. 4(b).

Observations reveal that the flux paths in the top and bottom limbs and the flux distribution vary depending on the primary and secondary magnetomotive forces (MMFs). To address this, this work develops a reluctance model for the top and bottom limbs, based on the assumption that, under unequal MMF conditions (Fig. 4(b)), the flux is evenly divided, occupying 50% of the cross-sectional area. Also, the reluctance of the inner flux path is assumed to be distributed in the ratio of 1:2 $\left(\frac{d_{pri}}{d_s} \text{ and } \frac{2d_{pri}}{d_s}\right)$. Considering the IMTx 1 design, the different core reluctances can be found using classical methods as follows:

Core reluctances of the U-core:

The reluctance associated with the U-core can be calculated directly based on the dimensions. The reluctances R_1, R_2 and R_3 as indicated in Fig. 4(c) are given by:

$$R_1 = \frac{w_s}{\mu_0\mu_r w_c d_c}$$
$$R_2 = \frac{0.25\pi w_c}{\mu_o\mu_r w_c d_c}$$
$$R_3 = \frac{d_s}{0.5\mu_0\mu_r w_c d_c}$$

Core reluctances of the I-core:

The reluctance associated with the introduction of the external leakage path, namely R_4, R_5, and R_6, are given by:

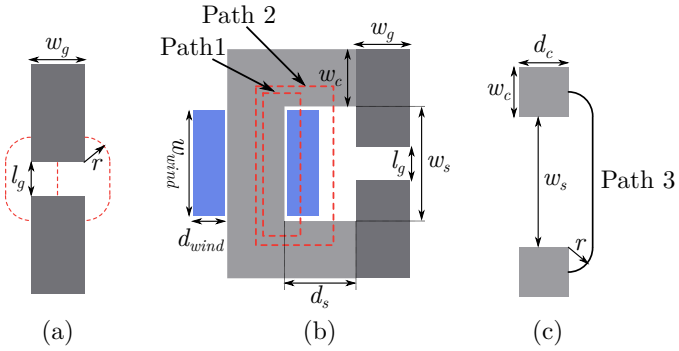

Fig. 5: Fringing and leakage flux paths (a) Fringing flux paths across an air-gap, R_g (b) Front view: vertical (Path 1 and 2) reluctance (c) Side view: vertical path (Path 3) [14]. R_{v1} and R_{v2} are calculated using Path 1,3 and Path 2,3 respectively.

$$R_4 = \frac{w_g}{0.5\mu_0\mu_r w_c d_c}$$
$$R_5 = \frac{0.5\pi}{\mu_0\mu_r d_c}\frac{(0.25w_g + 0.5w_c)}{(w_g + 0.5w_c)}$$
$$R_6 = \frac{w_s - l_g}{\mu_0\mu_r w_g d_c}$$

To have a minimum reluctance path for R_5, the radius is considered to be a mean of $0.5w_c$ and $0.25w_g$ (during case 1), resulting in a minimum mean magnetic path length. Similarly, the cross-sectional area is considered a mean of $0.5w_c d_c$ and $w_g d_c$ (during case 2), resulting in the maximum mean magnetic cross-sectional area. For all this core reluctance, the core material is assumed to operate in the linear range where

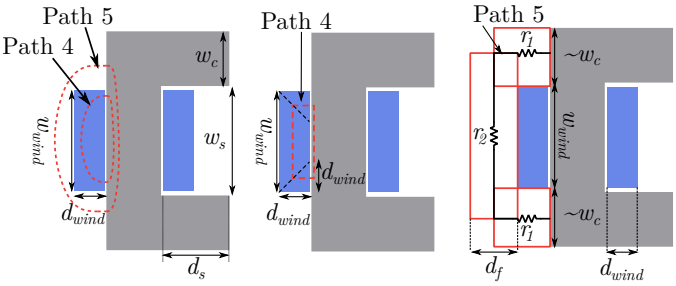

Fig. 6: (a) Face leakage paths through the winding and the air; (b) through the winding; (c) through the air [14]. R_f is calculated using Path 4, 5.

the relative permeability μ_r is constant.

Leakage reluctance:

Deriving the analytical expressions for each leakage reluctance path is difficult because of the curvature of the path that the leakage flux follows while exiting and entering the core. While the architecture of the magnetics greatly influences these leakages, the leakage reluctances shown in red can be approximated with some degree of accuracy using a few basic assumptions. There are two forms of leakage reluctance: window reluctance, as seen in Fig. 5(b)-(c), Fig. 6(a)-(c), and fringing reluctance, as seen in Fig. 5(a) due to an air gap. Window reluctances can be estimated by using the idea of $\mathrm{E} = \frac{1}{2}\mu \int_V H^2\, dV$, which represents the energy stored in a magnetically linear component and shows the relationship between the fields and the geometry [14].

B. MEC-based Design Algorithm for Leakage Integration

The energy stored in the leakage inductance of the transformer's windings directly relates to the field space between the primary and secondary windings. Higher energy relates to higher leakage inductance [7]. Thus, windings on separate limbs can, therefore, provide increased leakage. Additionally, by incorporating an external leakage path along an appropriate leakage path composed of the same or different grade of high-permeability ferrite material with an air gap, controlled leakage inductance can be achieved by modulating the air gap length l_g and width of the leakage path w_g. An integrated design prototype can be designed per the flowchart shown in Fig. 7.

The design algorithm requires system specifications such as kVA ratings (rms primary and secondary currents and voltage levels V_{in}, I_{prms} and V_o, I_{srms} respectively) and required leakage inductance L_{req}. An initial value of the I_{p1}, I_{p2}, I_{s1} and I_{s2} for limiting the observed peak flux density across the core below the maximum design peak flux density B_m. The design algorithm consists of two parts: (i) the design of a transformer without an external leakage path to set the magnetizing inductance, L_{m-tx} and (ii) the design of an external leakage path based on L_{req}. U-core geometry is selected to establish higher leakage inductance by placing the windings on different limbs. The core cross-sectional area A_c and window area A_w are selected using the area-product approach. n_1 and n_2 collectively refer to

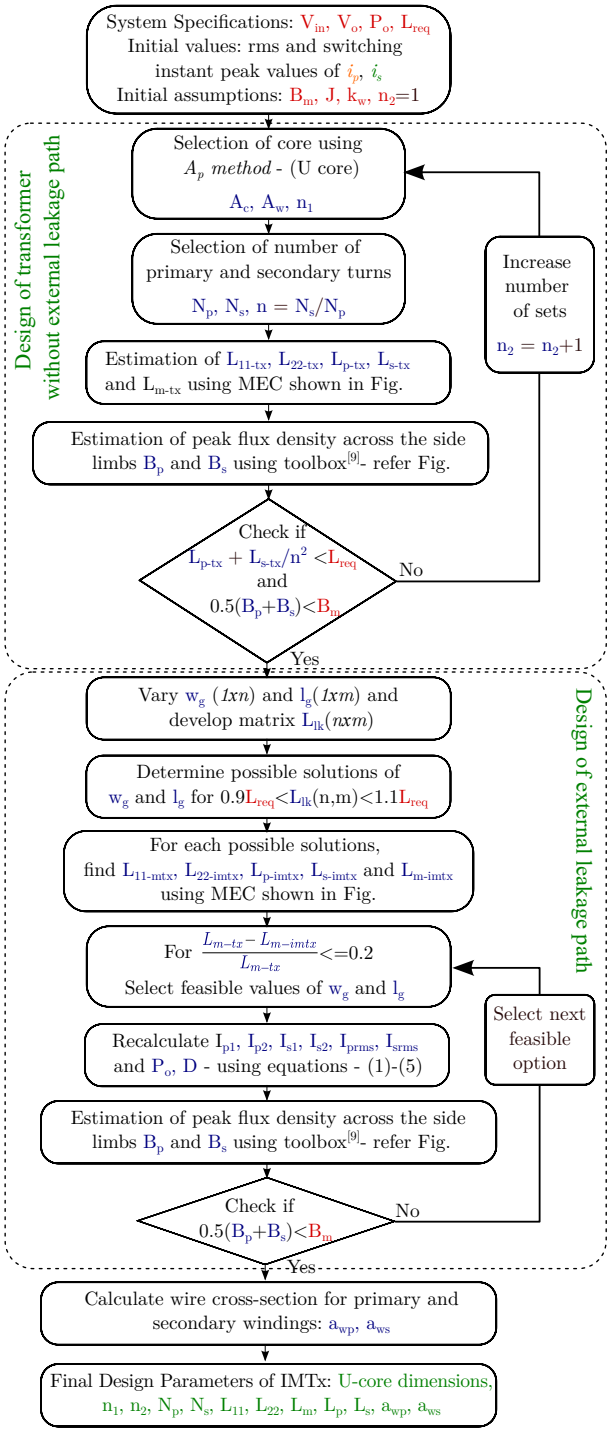

Fig. 7: Flowchart for MEC-based design algorithm for integrated magnetic transformer design.

the number of core sets. The primary and secondary leakage inductance L_{p-tx} and L_{s-tx}, respectively, in the first design step, are designed so that $L_{p-tx} + L_{s-tx}/n^2 < L_{req}$. This constraint is applied because when the external leakage path is included, this value will be the minimum attainable leakage inductance from the obtained magnetic structure. Once the core dimension and number of primary N_p and secondary N_s turns are set, the possible solution sets of width w_g

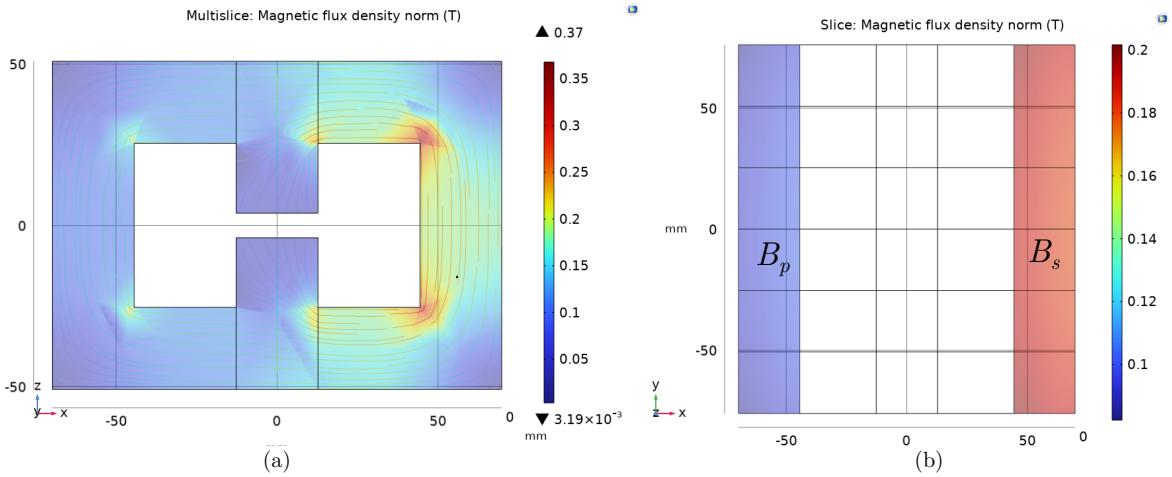

(a) (b)

Fig. 8: 3D FEA magnetostatic results showcasing magnetic flux density distribution design IMTx 1; for switching instant where $i_p(t)$ = I_{p1} and $i_s(t)$ = I_{s1} (refer to column 9, row 5 of Table I) (a) Front cross-sectional view (plane y=0) (b) Top cross-sectional view (plane z=0).

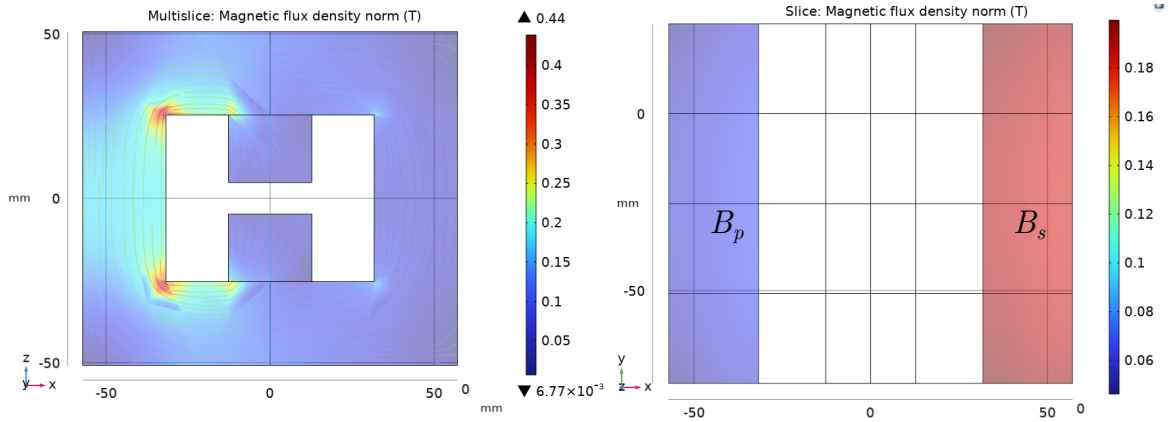

(a) (b)

Fig. 9: 3D FEA magnetostatic results showcasing magnetic flux density distribution design IMTx 2; for switching instant where $i_p(t)$ = I_{p2} and $i_s(t)$ = I_{s2} (refer to column 10, row 6 of Table I) (a) Front cross-sectional view (plane y=0) (b) Top cross-sectional view (plane z=0).

and air-gap length l_g that provide L_{req} are estimated. The magnetizing inductance L_{m-imtx} is constrained to be at least 80% of L_{m-tx}. With the inclusion of an external leakage path in IMTx 1, the magnetizing inductance will be lowered as opposed to IMTx 2, where it will remain unchanged. At each design stage, the observed peak flux density B_p and B_s as shown in Fig. 8(b) and 9(b) are estimated using [15] so that average flux density across the core cross-section is $<= B_m$. After design completion, the rms primary I_{prms} and secondary I_{srms} currents are estimated to select the proper wire cross-section a_{wp} and a_{ws} respectively.

IV. Simulation Results

To evaluate the magnetic performance and validate the accuracy of the proposed MEC model for designs indicated in Fig. 1, a 3D Finite Element Analysis (FEA) magnetostatic simulation was conducted using COMSOL Multiphysics. The study focused on two variations of IMTx design, utilizing a U-core geometry (U/100/57/25) and I-core (I/100/25/25) geometry modeled as the external leakage path. The I-cores were appropriately cut to include the air gap in the leakage path. The final design details are as follows (i) *Prototype IMTx 1*: $n_1 + n_2$ = 6, N_p = 8, N_s = 5, l_g = 7.6 mm and w_g = 25.4 mm, and (ii) *Prototype IMTx 2*: $n_1 + n_2$ = 4, N_p = 12, N_s = 8, l_g = 9.6 mm and w_g = 25.4 mm. To verify the proposed MEC model's efficacy, the 3D FEA simulation results were compared with the analytical MEC model results indicated in Table I. Fig. 8 and 9 shows the magnetic flux density distribution across the limb's cross-section under different MMF conditions. The Fig. 8(b) and 9(b) indicates the region where the average flux density observed across the cross-section of the core is estimated and denoted by B_{p1}, B_{s1}, and B_{p2} during the MMF condition of N_pI_{p1}, N_sI_{s1} and N_pI_{p2}, N_sI_{s2} as indicated switching instants in Fig. 3. The average flux density, $B_{av1} = \frac{B_{p1} + B_{s1}}{2}$ and $B_{av2} = \frac{B_{p2} + B_{s2}}{2}$ are observed to be below design value, B_m. The two results are in good agreement with around 10% deviation for prototype IMTx 1.

TABLE I: Comparison of MEC-based analytical and 3D FEA magnetostatic simulation results

Results	Design Parameters							Peak flux density observed at switching instants (Fig. 3)	
	Designs	$L_{11-imtx}$	$L_{22-imtx}$	L_{m-imtx}	$L_p - imtx$	$L_s - imtx$	L_{leakT}	I_{p1}, I_{s1} B_{p1}, B_{s1} B_{av1}	I_{p2}, I_{s2} B_{p2}, B_{s2} B_{av2}
MEC model	IMTx 1	1.96 mH	0.77 mH	1.20 mH	54.29 μH	21.21 μH	108.58 μH	25.13 A, 43.58 A 0.079 T, 0.186 T 0.132 T	24.19 A, 35.44 A 0.175 T, 0.081 T 0.128 T
	IMTx 2	3.42 mH	1.52 mH	2.25 mH	52.13 μH	23.17 μH	104.25 μH	25.84 A, 40.32 A 0.057 T, 0.172 T 0.115T	26.88 A, 38.75 A 0.172 T, 0.058 T 0.115T
3D FEA	IMTx 1	2.11 mH	0.83 mH	1.28 mH	53.61 μH	20.49 μH	107.1 μH	25.13 A, 43.58 A B_{av1} = 0.142 T	24.19 A, 35.44 A B_{av2} = 0.137 T
	IMTx 2	3.73 mH	1.66 mH	2.44 mH	73.29 uH	32.48 μH	146.36 μH	25.84 A, 40.32 A B_{av1} = 0.125 T	26.88 A, 38.75 A B_{av2} = 0.125 T

For the IMTx 2 design, the interaction of fringing reluctance and leakage reluctance paths (R_{v2}) is significant and not accounted for in this work; thus, the results show a significant difference. N87 material with a relative permeability of 2200 is assumed. The initial assumptions during the A_p method are peak flux density (B_m) of 0.14 T, current density (J) of $5A/mm^2$, and window utilization factor (k_w) of 0.4.

V. Conclusion

Compact, reliable, and efficient converter operation calls for innovative magnetic design approaches, and one solution is to go for integrated magnetic designs when multiple magnetic components are involved which could be coupled. Two integrated magnetic structures for a dual-active bridge converter that uses an improved magnetic equivalent circuit are presented in this work. An efficient design methodology that uses an iterative approach is proposed. The design iterations are minimized by utilizing and continuously improving the reluctance modeling. Maintaining the observed peak flux density below a threshold B_m is made possible by an improved analytical MEC model for the examined integrated magnetic structures, confirming the uneven flux distribution over the core structure under various MMF conditions.

Acknowledgment

The authors gratefully acknowledge 2023 IEEE PELS Graduate Studies Fellowship and the IEEE PELS John G. Kassakian Fellowship, and IISC-TU Delft Seed Fund Grant 2023 for supporting research collaboration and financial support. The authors also acknowledge the I-STEM portal for providing access to COMSOL Multiphysics software, which helped in performing the 3D FEA magnetostatic simulations.

References

[1] M. Kheraluwala, R. Gascoigne, D. Divan, and E. Baumann, "Performance characterization of a high-power dual active bridge DC-to-DC converter," *IEEE Transactions on Industry Applications*, vol. 28, no. 6, pp. 1294–1301, 1992.

[2] M. Li, Z. Ouyang, and M. A. E. Andersen, "High-Frequency LLC Resonant Converter With Magnetic Shunt Integrated Planar Transformer," *IEEE Transactions on Power Electronics*, vol. 34, no. 3, pp. 2405–2415, 2019.

[3] S. Cuk, "Coupled Inductor and Integrated Magnetics Techniques in Power Electronics," in *INTELEC '83 - Fifth International Telecommunications Energy Conference*, 1983, pp. 269–275.

[4] A. Witulski, "Introduction to modeling of transformers and coupled inductors," *IEEE Transactions on Power Electronics*, vol. 10, no. 3, pp. 349–357, 1995.

[5] V. Valdivia, J. Pleite, P. Zumel, and C. Gonzalez, "Improving the design of integrated magnetics for power electronics systems," in *2008 IEEE Power Electronics Specialists Conference*, 2008, pp. 2685–2690.

[6] E. S. Lee, J. H. Park, M. Y. Kim, and S. H. Han, "An Integrated Transformer Design With a Center-Core Air-Gap for DAB Converters," *IEEE Access*, vol. 9, pp. 121 263–121 278, 2021.

[7] M. Mu, L. Xue, D. Boroyevich, B. Hughes, and P. Mattavelli, "Design of integrated transformer and inductor for high frequency dual active bridge GaN Charger for PHEV," in *2015 IEEE Applied Power Electronics Conference and Exposition (APEC)*, 2015, pp. 579–585. [Online]. Available: https://ieeexplore.ieee.org/document/7104407

[8] B. Cougo and J. W. Kolar, "Integration of Leakage Inductance in Tape Wound Core Transformers for Dual Active Bridge Converters," in *2012 7th International Conference on Integrated Power Electronics Systems (CIPS)*, 2012, pp. 1–6.

[9] M. Meinhardt, M. Duffy, T. O'Donnell, S. O'Reilly, J. Flannery, and C. O Mathuna, "New method for integration of resonant inductor and transformer-design, realisation, measurements," in *APEC '99. Fourteenth Annual Applied Power Electronics Conference and Exposition. 1999 Conference Proceedings (Cat. No.99CH36285)*, vol. 2, 1999, pp. 1168–1174 vol.2.

[10] X. Chen, G. Xu, Q. Shen, Y. Sun, and M. Su, "Magnetizing and Leakage Inductance Integration for Split Transformers With Standard UI Cores," *IEEE Transactions on Power Electronics*, vol. 37, no. 11, pp. 12 980–12 985, 2022. [Online]. Available: https://ieeexplore.ieee.org/document/9798698

[11] M. Pavlovsky, S. W. H. de Haan, and J. A. Ferreira, "Winding losses in high-current, high-frequency transformer foil windings with leakage layer," in *2006 37th IEEE Power Electronics Specialists Conference*, 2006, pp. 1–7.

[12] D. Das and K. Basu, "Modulation Strategy to Minimise RMS and Peak Currents in Dual Active Bridge Converter," in *2020 IEEE Energy Conversion Congress and Exposition (ECCE)*, 2020, pp. 969–974.

[13] M. Pavlovsky, S. W. H. de Haan, and J. A. Ferreira, "Winding losses in high-current, high-frequency transformer foil windings with leakage layer," in *2006 37th IEEE Power Electronics Specialists Conference*, 2006, pp. 1–7.

[14] *Magnetics and Magnetic Equivalent Circuits*. John Wiley Sons, Ltd, 2021, ch. 2, pp. 43–101. [Online]. Available: https://onlinelibrary.wiley.com/doi/abs/10.1002/9781119674658.ch2

[15] Purdue University, School of Electrical and Computer Engineering, "Power Magnetic Material Toolbox." [Online]. Available: https://engineering.purdue.edu/ECE/Research/Areas/PES/Software/power_magnetic_material_toolbox